3D Radiation Pattern Reconstruction from Reduced Far-Field Sampling via Iterative Spectral Interpolation

Jake W. LIU

Dept. of Electronic Engineering, National Taipei University of Technology, Taipei, 10608, Taiwan

jwliu@ntut.edu.tw

Submitted November 18, 2025 / Accepted June 24, 2026 / Online first July 16, 2026

Abstract. *This paper presents a method for reconstructing the three-dimensional antenna radiation pattern from reduced sampled far-field measurements, thereby reducing the need for extensive mechanical probe scans. The sampling density is selected according to planar near-field measurement principles, enabling an initial plane-wave representation of the radiation field. An iterative interpolation procedure in the spectral domain is then used to recover the missing angular data while accounting for practical measurement resolution limits. The complete source code written in Julia programming language for the reconstruction algorithm is publicly available to support reproducibility and future research.*

Keywords

Antenna radiation, reconstruction algorithm, far-field pattern measurement, near-to-far field transformation

1. Introduction

Antenna radiation measurement is a labor-intensive and time-consuming process that typically requires numerous mechanical probe scans to fully characterize the radiation pattern [1–7]. The challenge becomes even more pronounced when multiple measurement loops are needed to analyze the beam-steering behavior of phased arrays or multi-beam antennas [8], [9].

In recent years, there has been a growing demand for using measured data to synthesize or calibrate radiation patterns of phased arrays at millimeter-wave (mmW) frequencies. This trend stems from the inherent phase uncertainties among radio-frequency (RF) devices, which require iterative refinement of the radiation pattern during the synthesis or calibration process. Approaches such as genetic algorithms (GA) and the successive projection method (SPM) have been widely adopted to improve efficiency in these tasks [10–13].

Parallel to these developments, significant effort has been devoted to reducing the measurement burden while maintaining high pattern accuracy. Compressive sensing methods have enabled far-field radiation pattern reconstruction from a limited set of random samples by exploiting sparsity in Fourier or cosine transform domains [14]. Deep learning techniques have also emerged as powerful tools, with recent works demonstrating near-field acceleration using neural networks such as the Near-field Super-resolution Network (NFS-Net), which reconstructs high-resolution fields from substantially undersampled data [15]. Additionally, pattern reconstruction from phaseless measurements in reverberation chambers has been achieved by extracting spherical wave coefficients using power correlation and nonlinear optimization techniques [16]. Collectively, these advances reflect a clear shift toward more efficient and flexible characterization methodologies that mitigate the constraints of traditional mechanical measurement systems.

In this work, we propose a method to reconstruct the three-dimensional (3D) far-field radiation pattern from sampled far-field data using spectral-domain (k-domain) sampling. The sampling density is determined from planar near-field measurement theory to ensure that the radiation pattern is well represented by a plane-wave expansion [17–20]. The reduced measured field is transformed into the spectral domain, where an iterative interpolation procedure is used to estimate the missing components. Through successive refinement of the spectral estimate, the complete radiation pattern can be accurately recovered while maintaining consistency with the available measurements. This approach significantly reduces the number of required sampling points without degrading accuracy, providing a practical alternative to conventional exhaustive probe scanning.

Relative to our prior work on PSTD-based near-to-far-field transformation with sinc interpolation [21], this paper (i) targets direct 3D far-field reconstruction from reduced far-field sampling rather than from simulated near-field data, (ii) formalizes the measurement-set construction via aperture-driven spectral sampling with explicit $\mathcal{M}/\mathcal{R}$ partitioning and a cost-based stopping rule, and (iii) provides experimental compact-antenna-test-range validation together with open-source Julia implementation. We also clarify that dense far-field grids remain necessary for high-fidelity diagnostics, beam-pointing accuracy, and pattern-synthesis or compliance

DOI: 10.13164/re.2026.0365

tasks even when a minimally sufficient set of samples exists for coarse characterization.

The remainder of this paper is organized as follows. Section 2 outlines the theoretical foundation of the proposed approach based on planar near-field principles. Section 3 describes the reconstruction algorithm, derives the implementation criteria, and discusses practical considerations. Section 4 presents numerical and experimental results to validate the method. Section 5 concludes the paper with a brief discussion. An $\exp(\mathrm{i}\omega t)$ time convention is assumed and omitted throughout.

2. Summary of the Theoretical Basis

Sections 2.1 and 2.2 establish the spectral-domain framework used for reconstructing 3D far-field radiation patterns from reduced sampled measurements. Section 2.1 formulates the electromagnetic field in terms of its plane-wave spectrum and identifies the associated sampling constraints dictated by spatial bandwidth. This analysis provides the basis for determining the minimum required sampling density in the angular domain. Section 2.2 then links the spectral representation to the far-field radiation pattern through asymptotic evaluation of the plane-wave expansion, enabling an inverse reconstruction strategy.

Unlike traditional near-to-far-field (NTFF) transformations, which propagate complete near-field data forward to determine the far-field pattern, the proposed approach begins by identifying the minimum number of far-field samples needed to capture the essential spectral content of the field. The reconstruction problem is therefore formulated as a spectral-domain completion task, enabling efficient recovery of the 3D radiation pattern from reduced measurements.

2.1 Plane-Wave Spectrum Representation of the Electromagnetic Field

The far-field radiation of an antenna can be expressed as a superposition of plane waves. This representation, known as the plane-wave spectrum (PWS), provides a natural basis for characterizing spatial electromagnetic fields in homogeneous media. In this work, the electric field is projected onto a two-dimensional spectral domain defined by the

$$k_x = k_0 \sin\theta\cos\phi, k_y = k_0 \sin\theta\sin\phi \tag{1}$$

where $k_0 = 2\pi/\lambda$ is the free-space wavenumber.

The total electric field $\vec{E}(x, y, z)$ can be synthesized from its spectral content as

$$\vec{E}(x, y, z) = \iint_{-\infty}^{\infty} \vec{\mathcal{E}}(k_x, k_y, z) \mathrm{e}^{-\mathrm{i}(k_x x + k_y y)}\, \mathrm{d}k_x\, \mathrm{d}k_y \tag{2}$$

where the spectral field is given by the inverse transform

$$\vec{\mathcal{E}}(k_x, k_y, z) = \frac{1}{4\pi^2} \iint_{-\infty}^{\infty} \vec{E}(x, y, z) \mathrm{e}^{\mathrm{i}(k_x x + k_y y)}\, \mathrm{d}x\, \mathrm{d}y. \tag{3}$$

Equations (2) and (3) form a two-dimensional Fourier transform pair. These expressions establish the theoretical rationale for selecting appropriate sampling densities in the far-field or near-field domains.

To identify the spectral sampling constraints, consider the antenna aperture located at $z = 0$. If the aperture field is spatially sampled on a grid with spacing

$$\Delta\xi = \frac{\pi}{k_0} = \frac{\lambda}{2}, \qquad \xi = x \vee y \tag{4}$$

then the resulting discrete spectrum captures all propagating components satisfying $|k_x| \le k_0$ and $|k_y| \le k_0$. The choice of half-wavelength spacing ensures that the dominant spectral content is preserved while avoiding aliasing.

The corresponding sampling intervals in the spectral domain are

$$\Delta k_x = \frac{2\pi}{L_x}, \qquad \Delta k_y = \frac{2\pi}{L_y} \tag{5}$$

where L_x and L_y denote the physical aperture dimensions in the x- and y-directions, respectively. Although reduced sampling may result in an incomplete set of spectral samples, proper selection of spatial sampling intervals ensures that the available data remain sufficient to reconstruct the full plane-wave spectrum. This motivates the subsequent discussion on connecting the spectral field to the far-field radiation pattern.

2.2 Asymptotic Relation Between the Spectral Field and Far-Field Radiation

The connection between the plane-wave spectrum and the observable far-field radiation pattern is obtained by asymptotically evaluating (2) in the limit $r \to \infty$. In the radiation zone ($r \gg \lambda$), the far-field electric field can be approximated as

$$\vec{E}_{\mathrm{FF}}(r, \theta, \phi) \approx C(k_0, r)\, \cos\theta\, \vec{\mathcal{E}}(k_x, k_y) \tag{6}$$

where (k_x, k_y) are defined by (1), and

$$C(k_0, r) = \frac{2\pi i k_0}{r} \mathrm{e}^{-\mathrm{i}k_0 r} \tag{7}$$

is the asymptotic spherical-wave factor governing the $1/r$ decay.

This expression provides a direct link between the spectral-domain representation and the far-field pattern. Traditional planar NTFF methods rely on forward propagation from a densely sampled near-field distribution. In contrast, the present work adopts the inverse perspective: we begin by identifying the minimum number of far-field samples necessary to capture the essential spectral content of the field, using (1) to (6) as the guiding relations.

Holographic and back-propagation approaches are not restricted to near-field starting data: when critically sampled far-field data are available, particularly for planar or aperture antennas, the plane-wave spectrum can be obtained directly via FFT/DFT, and the far field can then be computed at any direction without iteration [17], [22]. Likewise, in spherical near-field measurements the field is acquired at close-to-critical angular sampling dictated by the electrical size of the antenna; after extraction of the vector spherical-harmonic coefficients the far field follows at arbitrary directions [23]. The proposed method addresses a complementary scenario: the far-field set $\mathcal{M}$ is deliberately kept smaller than the critically sampled set that these established techniques would require, and the missing spectral information is recovered iteratively. This reduces the total number of measurements at the expense of an inexpensive post-processing step. Moreover, performing the interpolation in the spectral domain (k_x, k_y) rather than directly in the angular domain (θ, ϕ) exploits the band-limiting imposed by the finite aperture and produces smoother reconstructions, as demonstrated in Sec. 4.

Once these far-field sampling points are determined, the reconstruction task becomes one of spectral completion: the available samples are transformed into the spectral domain and iteratively interpolated to recover the missing components. This procedure dramatically reduces the number of required measurements while preserving accuracy. Although the formulation is naturally suited to the forward (positive) hemisphere, it can be applied equally well to the backward hemisphere.

In the next section, we provide a detailed description of the iterative reconstruction method built upon the theoretical foundation developed above.

3. Reconstruction Algorithm

This section describes the implementation of the proposed far-field reconstruction algorithm. The method consists of two key stages: (i) determining the far-field sampling points required to capture the essential spectral content of the antenna radiation, and (ii) reconstructing the complete far-field pattern through an iterative interpolation procedure conducted in the spectral domain.

3.1 Determination of Radiation Measurement and Recovery Points

Reconstructing the full three-dimensional radiation pattern from a limited set of measured samples requires identifying the appropriate angular sampling locations where far-field data must be acquired. This sampling scheme is derived from the spectral-domain analysis in Sec. 2, which establishes a correspondence between spatial sampling on the aperture and angular sampling in the far field via the PWS.

We assume that the effective radiating aperture is confined within a rectangular region of size $L_x \times L_y$. From the spatial sampling criterion for accurate spectral representation, the sampling interval on the aperture must satisfy the half-wavelength condition in (4). To determine the required far-field sampling points, we select a spectral-domain sampling interval

$$\Delta k_x = \Delta k_y = \Delta k = \frac{2\pi}{L} \tag{8}$$

where $L > \max\{L_x, L_y\}$ ensures that the aperture is fully enclosed by a larger square support region.

This leads to the discretized spectral sampling locations

$$k_{x,m} = \frac{2\pi}{L}m, \qquad k_{y,n} = \frac{2\pi}{L}n \tag{9}$$

where

$$m, n = -\left\lceil \frac{N-1}{2} \right\rceil : 1 : \left\lfloor \frac{N-1}{2} \right\rfloor, \qquad N = \left\lfloor \frac{2k_0}{2\pi/L} \right\rfloor.$$

Only spectral points satisfying $k_{x,m}^2 + k_{y,n}^2 \le k_0^2$ are retained, as points outside this circle correspond to evanescent waves and do not contribute to the far-field pattern.

Using the mapping in (1), the angular measurement points follow as

$$\begin{aligned} \theta_{mn} &= \arcsin\sqrt{\left(\frac{k_{x,m}}{k_0}\right)^2 + \left(\frac{k_{y,n}}{k_0}\right)^2}, \\ \phi_{mn} &= \operatorname{atan2}(k_{y,n}, k_{x,m}) \end{aligned} \tag{10}$$

where the four-quadrant inverse tangent is used for ϕ_{mn} to ensure correct angular placement.

To facilitate reconstruction, the angular domain is partitioned into:

- **Measurement region** $\mathcal{M}$: the set of angular points at which the far-field is actually measured,
- **Recovery region** $\mathcal{R}$: the remaining angular points for which the far-field must be reconstructed.

The union $\mathcal{F} = \mathcal{M} \cup \mathcal{R}$ defines the complete 3D angular region of interest.

In an ideal setting, once the points in $\mathcal{M}$ are known, the missing data in $\mathcal{R}$ could be directly reconstructed using (6) via sinc interpolation. However, practical measurements are constrained by the angular resolution of the equipment. Therefore, the coordinates derived from (10) are rounded to the nearest available resolution:

$$(\theta_{mn}, \phi_{mn}) \approx (\theta_{\mathcal{M}}, \phi_{\mathcal{M}}) \tag{11}$$

where $(\theta_{\mathcal{M}}, \phi_{\mathcal{M}})$ denote the angular locations at which measurements are actually taken. The remaining points $(\theta_{\mathcal{R}}, \phi_{\mathcal{R}})$ constitute the recovery region. A graphical illustration of the sampling process implied by (9)–(11) is provided in Fig. 1.

For clarity, the measurement set $\mathcal{M}$ is built in practice by: 1) computing the aperture grid with $\Delta\xi = \lambda/2$ and size (L_x, L_y), 2) mapping every retained spectral grid point $(k_{x,m}, k_{y,n})$ within $k_x^2 + k_y^2 \le k_0^2$ to (θ_{mn}, ϕ_{mn}), 3) rounding to the instrument's angular resolution to obtain $(\theta_{\mathcal{M}}, \phi_{\mathcal{M}})$, and 4) assigning the remaining angular points to $\mathcal{R}$.

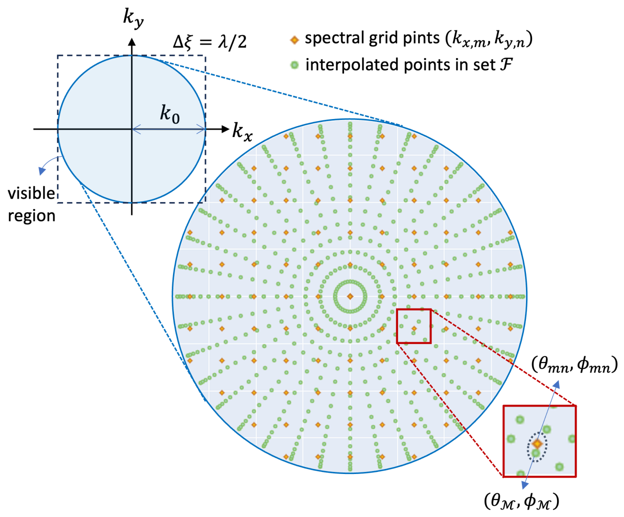

Fig. 1. Sampling structure in the spectral domain. The visible region is bounded by $k_x^2 + k_y^2 \le k_0^2$. Aperture dimensions (L_x, L_y) set Δk via (8), while the half-wavelength aperture spacing $\Delta\xi = \lambda/2$ sets the spectral span. Orange diamonds mark the discrete spectral grid points $(k_{x,m}, k_{y,n})$; green circles denote the measurement set $\mathcal{M}$ in the angular domain. The full angular set $\mathcal{F} = \mathcal{M} \cup \mathcal{R}$ (with $\mathcal{R}$ not shown) is linked to the spectral grid through the mapping $(k_{x,m}, k_{y,n}) \to (\theta_{mn}, \phi_{mn}) \approx (\theta_{\mathcal{M}}, \phi_{\mathcal{M}})$ according to (10) and (11).

3.2 Iterative Interpolation Procedure

The reconstruction of the complete 3D radiation pattern from sampled data is carried out via an iterative spectral-domain interpolation method. This approach exploits the smoothness and band-limited nature of the spectral field imposed by the finite antenna aperture. Working in the spectral domain is physically motivated because the finite aperture enforces spectral smoothness; bicubic spline interpolation preserves C^1 continuity in both magnitude and unwrapped phase, which stabilizes the back-mapping to (θ, ϕ). A simpler alternative would be to interpolate the $\mathcal{M}$ samples directly in the angular domain, e.g., by applying linear or spline interpolation along each ϕ-cut in the θ direction. However, such an approach does not exploit the spectral band-limiting imposed by the aperture and can only interpolate between existing samples on a given cut; it cannot recover information from neighboring cuts. The spectral-domain method, by contrast, couples all available measurements through the (k_x, k_y) representation. A numerical comparison is provided in Sec. 4.

The algorithm alternates between: (i) angular domain (θ, ϕ), where measurements are defined, and (ii) the spectral domain (k_x, k_y), where the field is interpolated. The main steps are summarized below.

1) Initialization The complex far-field components $E_\theta(\theta_\mathcal{M}, \phi_\mathcal{M})$ and $E_\phi(\theta_\mathcal{M}, \phi_\mathcal{M})$ are first obtained from measurement. Using (6), these values are mapped to spectral-domain samples and converted into Cartesian components $(\mathcal{E}_x, \mathcal{E}_y)$. Values at recovery locations $(\theta_\mathcal{R}, \phi_\mathcal{R})$ are initialized to zero.

A binary mask is defined as

$$\mathbf{M}(\theta_\mathcal{F}, \phi_\mathcal{F}) = \begin{cases} 1, & \text{if } (\theta_\mathcal{F}, \phi_\mathcal{F}) \in \mathcal{M}, \\ 0, & \text{if } (\theta_\mathcal{F}, \phi_\mathcal{F}) \in \mathcal{R}. \end{cases} \tag{12}$$

2) Forward mapping to the spectral domain The angular-domain Cartesian fields $\mathcal{E}_x(\theta_\mathcal{F}, \phi_\mathcal{F})$ and $\mathcal{E}_y(\theta_\mathcal{F}, \phi_\mathcal{F})$ are interpolated onto the spectral grid defined in (9) using scattered-data interpolation [24]. Magnitudes and phases are treated separately, with phase unwrapped following [25]. This yields estimates of $\mathcal{E}_x(k_{x,m}, k_{y,n})$ and $\mathcal{E}_y(k_{x,m}, k_{y,n})$ on the regular grid.

3) Smoothing and spectral interpolation The spectral samples are processed using bicubic spline interpolation to obtain continuous representations over the k-domain. These interpolated fields are then evaluated at the coordinates corresponding to the angular grid $(\theta_\mathcal{F}, \phi_\mathcal{F})$.

4) Data consistency enforcement Within the measurement region, the interpolated data are replaced by the original measurements:

$$\vec{\mathcal{E}}_{p+1}(\theta_\mathcal{F}, \phi_\mathcal{F}) = \mathbf{M} \odot \vec{\mathcal{E}}_0(\theta_\mathcal{F}, \phi_\mathcal{F}) + (1 - \mathbf{M}) \odot \vec{\mathcal{E}}_p(\theta_\mathcal{F}, \phi_\mathcal{F}) \tag{13}$$

where p is the iteration index, $\odot$ is the Hadamard product, and $\vec{\mathcal{E}}_0$ denotes the measured field.

5) Convergence criterion Convergence is monitored via the component-wise cost function

$$\mathrm{cost}_{\xi,p+1} = \frac{\sqrt{\sum_F \left| |\mathcal{E}_{\xi,p+1}|^2 - |\mathcal{E}_{\xi,p}|^2 \right|}}{\sqrt{\sum_F |\mathcal{E}_{\xi,p}|^2}}, \qquad \xi \in \{x, y\}, \tag{14}$$

and the total cost is

$$\mathrm{cost}_{p+1} = \mathrm{cost}_{x,p+1} + \mathrm{cost}_{y,p+1}. \tag{15}$$

The process terminates when the change in the total cost cost_{p+1} falls below a threshold ϵ or when a maximum iteration count is reached.

6) Inverse mapping to the far field Upon convergence, the updated spectral fields are mapped back to the far field using (6), yielding reconstructed Cartesian components that are subsequently converted to spherical components $E_\theta(\theta_\mathcal{F}, \phi_\mathcal{F})$ and $E_\phi(\theta_\mathcal{F}, \phi_\mathcal{F})$.

This iterative process maintains consistency with measured data while progressively refining the missing spectral components. The algorithm exploits spatial-spectral duality to achieve accurate reconstruction under reduced angular sampling. A summary of the workflow is shown in Fig. 2.

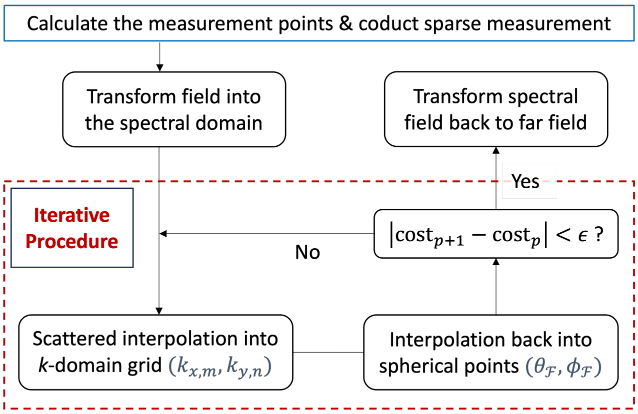

Fig. 2. Flowchart of the iterative reconstruction: 1) select $\mathcal{M}$ and acquire far-field samples, 2) map to the k-domain grid $(k_{x,m}, k_{y,n})$, 3) interpolate and smooth, 4) enforce data consistency on $\mathcal{M}$, and 5) iterate until the cost threshold is met before mapping back to the far field.

3.3 Computational Note

Equations (8) and (9) reveal that the choice of L directly controls the sampling density in the k-domain and, consequently, the number of far-field measurement points required through (10). In principle, one may choose L equal to the physical aperture size, which would suffice under ideal conditions without edge diffraction. However, in practical settings, accurate reconstruction of fine spatial features–particularly nulls and sidelobes–requires more conservative sampling.

For this reason, we adopt $L = 2\max\{L_x, L_y\}$, effectively doubling the aperture coverage and improving robustness to spectral leakage. The parameter N, determining the number of samples along each axis, is selected as an odd number to ensure inclusion of the boresight direction, which is typically of primary interest in radiation characterization.

4. Numerical and Experimental Validation

This section presents both simulated and measured results to validate the effectiveness of the proposed reconstruction method. The numerical examples demonstrate the theoretical consistency of the algorithm, while the experimental measurements confirm its practical applicability under realistic conditions. All numerical implementation and data processing were performed using the Julia programming language. Although the reduced set $\mathcal{M}$ is sufficient for coarse characterization, the reconstructed dense grids are used here to support diagnostics (e.g., sidelobe quantification), beam-pointing checks, and pattern synthesis where a 1° grid is still desirable. On principal-plane cuts (E- and H-plane), the measurement set $\mathcal{M}$ happens to provide moderate angular density, so the reconstructed curve appears to add only incremental detail. The reconstruction becomes more valuable on off-principal-plane cuts, where $\mathcal{M}$ provides very few samples and direct angular-domain interpolation fails to capture the sidelobe structure (see Sec. 4.1, Fig. 7). Additionally, the full 3D reconstruction enables computation of integrated quantities such as directivity, half-power beamwidth, and cross-polarization discrimination that require dense angular coverage beyond what the sparse set alone can provide.

4.1 Simulation Validation

In the numerical study, the proposed reconstruction procedure is first applied to a standard gain horn (SGH) antenna with a cross-sectional size of 70.00 mm × 57.67 mm, simulated at 35 GHz. The antenna structure is shown in Fig. 3. The simulated full 3D radiation pattern, sampled at 1° resolution in both θ and ϕ, is used as the reference for validation.

Following the sampling strategy in Sec. 3.3, a 37 × 37 aperture grid with half-wavelength spacing is adopted. Through the mapping in (10), and excluding nonphysical points associated with complex-valued angles, this grid corresponds to a total of 1220 far-field measurement points. In contrast, a full forward-hemisphere measurement with 1° sampling requires 180 × 181 = 32,580 data points. Thus, the proposed method uses only 1220/32,580 ≈ 3.7% of the full sampling requirement while still enabling accurate reconstruction of the 3D radiation pattern.

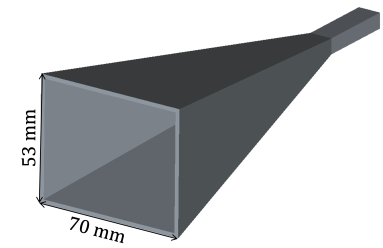

Fig. 3. Geometry of the SGH antenna used in the numerical validation. The antenna is simulated at 35 GHz.

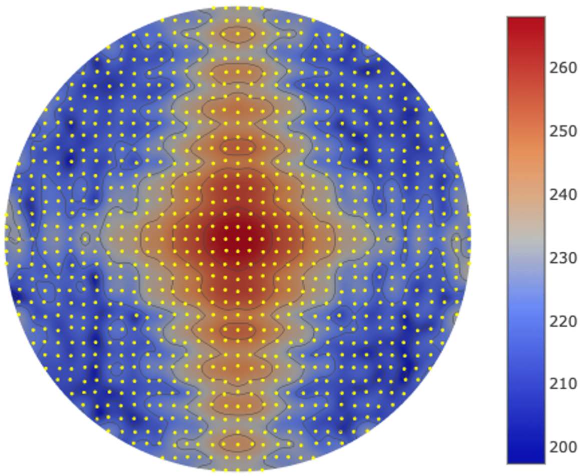

Fig. 4. Spectral field intensity of the SGH (dB scale with colorbar and labeled k_x, k_y axes). The contour plot denotes the reference data, and the yellow dots represent the samples required for the iterative reconstruction process.

The reference spectral field intensity, $\|\vec{\mathcal{E}}\|^2$ (in logarithmic scale), and the selected sampling locations in the k-domain are shown in Fig. 4. The contour plot represents the reference field distribution, while the yellow dots mark the reduced sampling points used as input to the reconstruction algorithm. The objective is to recover the full radiation field from these limited measurements, thereby validating the ability of the method to interpolate the missing spectral content.

The reconstructed 3D directivity pattern is shown in Fig. 5 and provides an overall visualization of the recovered far-field distribution. This result offers a heuristic validation of the reconstruction algorithm by illustrating that the global radiation characteristics can be accurately recovered from reduced samples.

A more detailed comparison is provided in Fig. 6, where the extracted 2D directivity patterns in the E-plane and H-plane are shown. These planar cuts are not directly measured; instead, they are derived from the reconstructed 3D pattern. The black dash-dotted curves denote the full-wave reference simulations, while the solid blue curves correspond to the reconstructed results. While discrepancies appear in deeper nulls away from boresight and in some secondary sidelobe details, the reconstructed patterns accurately capture the main beam and dominant sidelobe peaks. This level of agreement demonstrates that the essential features of the radiation pattern can be reliably recovered from reduced far-field sampling.

For comparison, Figure 6 also includes the result of direct angular-domain interpolation (dashed red), obtained by linearly interpolating the $\mathcal{M}$ samples along each ϕ-cut in the θ direction without any spectral-domain processing.

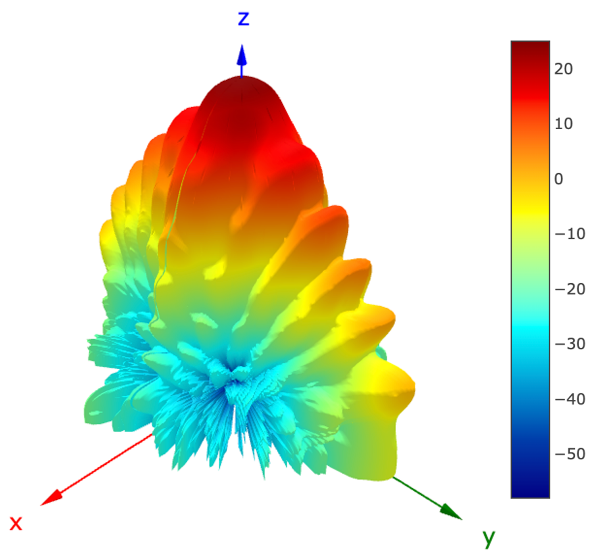

Fig. 5. Reconstructed 3D radiation pattern (directivity in dB scale) obtained using the proposed iterative method. The pattern is synthesized from reduced far-field samples and visualized to illustrate the directional characteristics of the recovered field over the entire forward hemisphere.

The spectral-domain reconstruction captures more sidelobe and null detail, particularly beyond $\theta \approx 30°$, and remains valid over the full angular range even where the $\mathcal{M}$ samples on a given cut become sparse or absent.

To further illustrate the practical benefit of the reconstruction, Figure 7 shows an off-principal-plane cut at $\phi = 45°$. Along this cut, the measurement set $\mathcal{M}$ contains significantly fewer samples than on the E- or H-plane, exposing the difference between interpolation strategies. The spectral-domain result (solid blue) follows the reference pattern more closely through the sidelobe region, whereas the direct angular-domain interpolation (dashed red) smoothly connects the available $\mathcal{M}$ samples but misses sidelobe detail between them and loses coverage where $\mathcal{M}$ samples become sparse at wider angles. For the present sampling geometry, the $\phi = 45°$ cut contains substantially fewer sampled angles than the principal-plane cuts, and beyond about $\theta \approx 55°$ only a few sampled points remain on that cut.

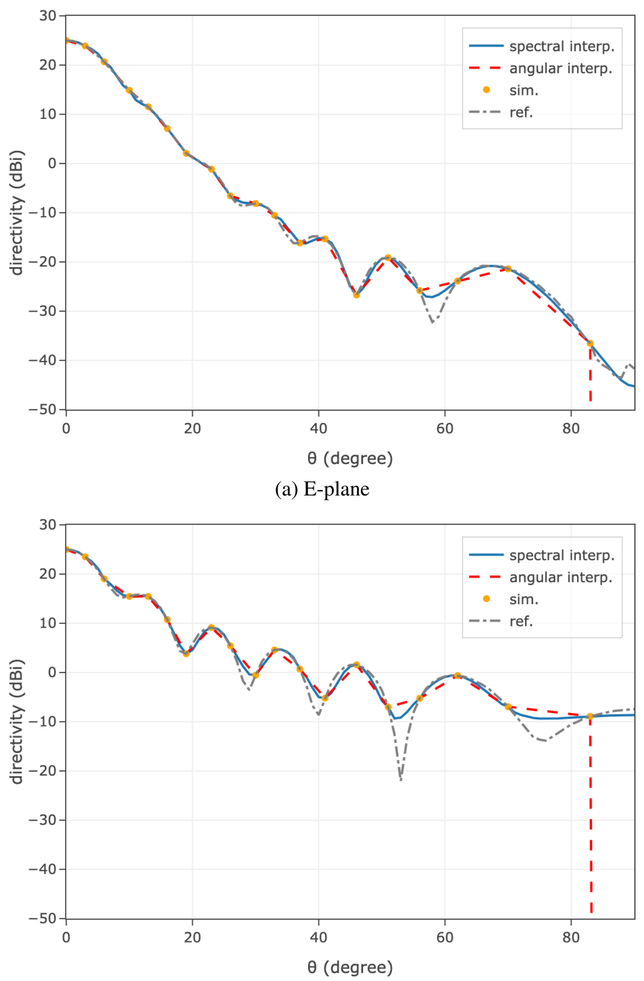

(a) E-plane

(b) H-plane

Fig. 6. Reconstructed 2D radiation patterns in the E-plane and H-plane. The dash-dotted black curves represent the reference data obtained from full-wave simulation. The orange dots denote the sampled far-field set $\mathcal{M}$ (simulation), the solid blue lines show the spectral-domain interpolation result, and the dashed red lines show the direct angular-domain interpolation for comparison.

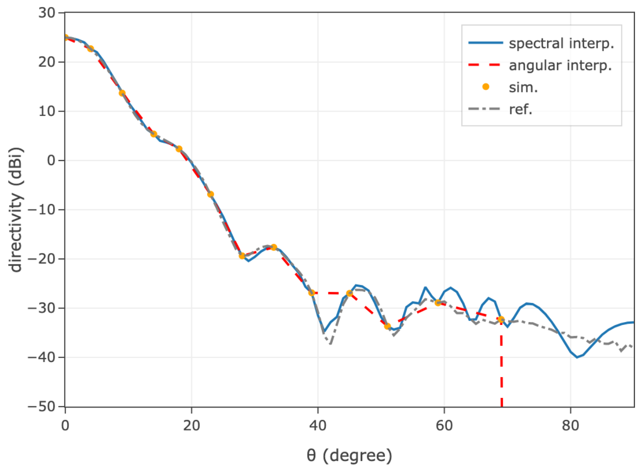

Fig. 7. Off-principal-plane radiation pattern cut at $\phi = 45°$ (simulation). The spectral-domain interpolation (solid blue) follows the reference (dash-dotted black) more closely than the direct angular-domain interpolation (dashed red), while weak artificial sidelobe appear beyond about $\theta \approx 55°$ where the cut becomes sparsely sampled.

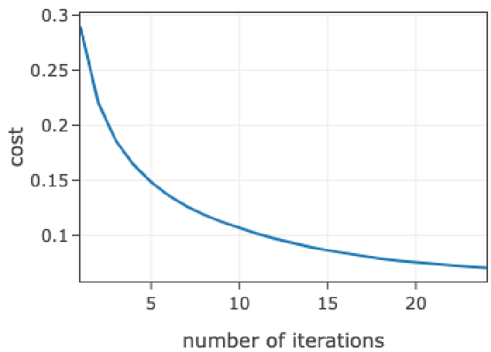

Fig. 8. Convergence of the iterative reconstruction algorithm. The cost function progressively decreases over iterations, indicating stable convergence toward a consistent solution that agrees with the measured data.

The weak artificial sidelobe structure in this region is therefore attributed conservatively to the limited support available at large angles, together with the discrete remapping/interpolation used in the current implementation when transferring data between the angular and spectral grids. In this low-level region, even small absolute reconstruction errors become more visible on the dB scale. This example shows that the proposed method can recover a denser off-axis reconstruction from the reduced samples through the spectral-domain reconstruction using all available samples, while also clarifying the present limitation of the method at the largest observation angles.

The convergence behavior of the iterative algorithm is shown in Fig. 8. For this example, the stopping threshold is set to $\epsilon = 10^{-3}$, corresponding to a relative change of 0.1%, and the reconstruction process converges at the 24th iteration. Although an optimal threshold value has not yet been fully established, the observed monotonic and rapid convergence suggests that the iterative procedure is both efficient and numerically stable. The average runtime of the algorithm, measured using the `BenchmarkTools.jl` package, is approximately 890 ms on a MacBook Air with an Apple M3 processor and 24 GB of RAM. This computation time is negligible compared to the time required for actual far-field data acquisition, making the algorithm well suited for integration within practical measurement workflows.

4.2 Experimental Validation

For experimental verification, the same SGH antenna used in the numerical example is measured in a compact antenna test range (CATR), as shown in Fig. 9. The CATR provides a controlled environment for accurate far-field measurements, and the experimental setup is configured to match the simulation parameters to enable direct comparison. The frequency, sampling configuration, and angular resolution are all kept consistent with the numerical validation.

The reconstructed 2D radiation patterns derived from experimental measurements are shown in Fig. 10. Following the same procedure as in the numerical case, the E-plane and H-plane cuts are extracted from the reconstructed 3D pattern. The reconstructed curves (blue) are compared against reference measurement data (dashed black). As observed in simulation, excellent agreement is obtained for the main beam and primary sidelobe regions. Some deviations occur in deep nulls and minor sidelobes due to measurement uncertainties and environmental factors inherent to practical test range setups. Nevertheless, the overall agreement verifies the robustness of the reconstruction method for real far-field data. As in the simulation case, the same trend holds for the experimental data: spectral-domain interpolation yields smoother sidelobe recovery than direct angular-domain interpolation (cf. the comparison in Figs. 6 and 7).

A full 3D far-field reference measurement covering the forward hemisphere with 1° resolution for both polarizations requires approximately three hours of acquisition time in the CATR In contrast, the reduced measurement corresponding to the proposed sampling strategy requires only about

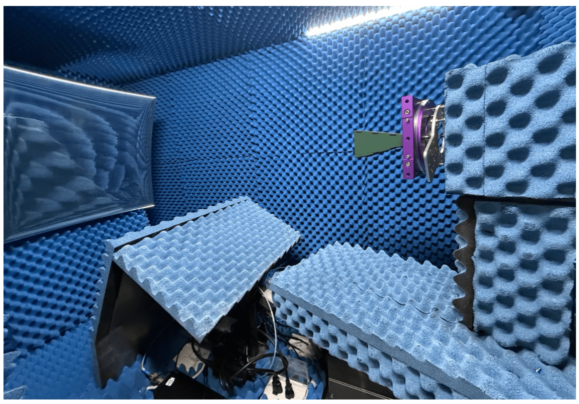

Fig. 9. Experimental setup for far-field measurement. The SGH antenna under test is mounted in a CATR system (Ohmplus Technology, OHMPLUS CATR-60H).

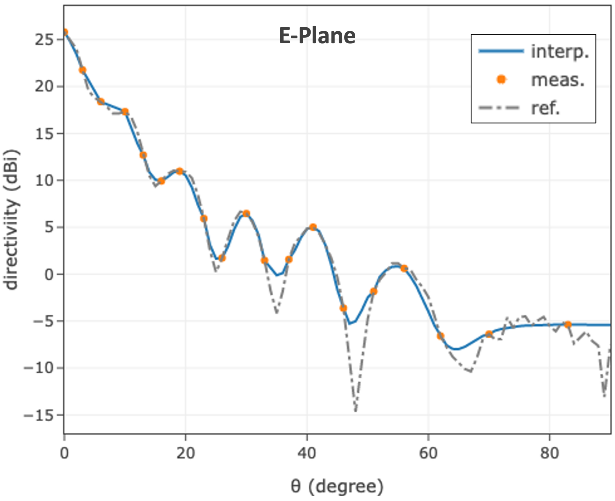

(a) E-plane

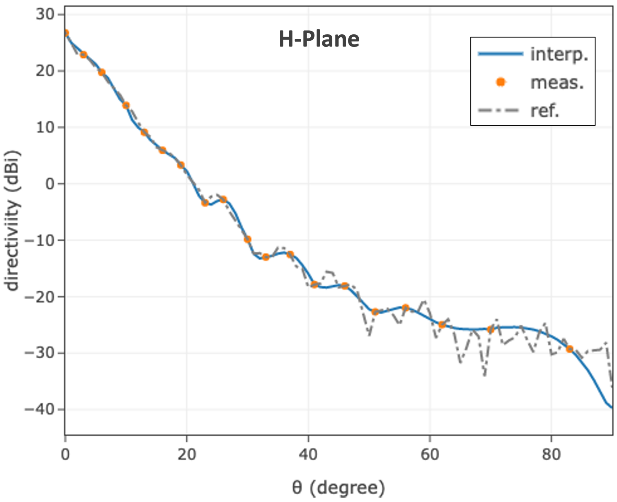

(b) H-plane

Fig. 10. Reconstructed 2D radiation patterns based on experimental measurements in the E-plane and H-plane. The dash-dotted black curves represent the reference patterns obtained from full pattern measurement, while the solid blue lines show the reconstructed results using the proposed iterative method. The orange dots indicate the reduced far-field samples $\mathcal{M}$ acquired during the measurement.

seven minutes, approximately 4% of the time required for a full measurement. This significant reduction highlights the practical utility of the proposed reconstruction method in accelerating antenna characterization procedures.

The reconstructed 3D radiation pattern based on experimental data is shown in Fig. 11. This result provides a comprehensive visualization of the recovered far-field structure. The main beam direction, overall radiation shape, and dominant sidelobe characteristics are faithfully recovered, closely matching the expected reference behavior. Despite using only a reduced subset of the far-field data, the reconstructed pattern exhibits high fidelity, demonstrating the method's capability to retrieve essential radiation features in realistic measurement scenarios.

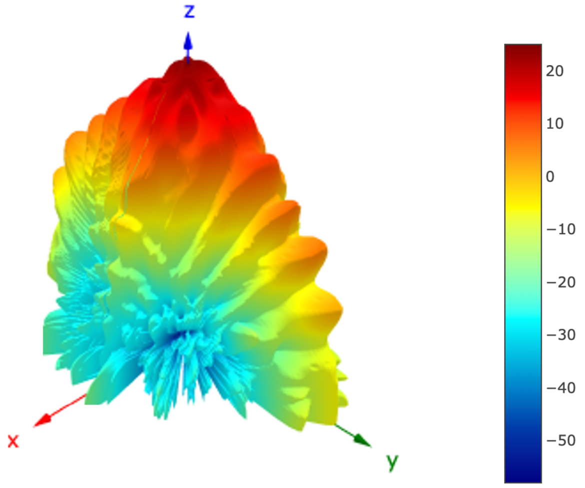

Fig. 11. Reconstructed 3D radiation pattern (directivity in dB) from experimental far-field measurements.

5. Conclusion

This paper has presented a method for reconstructing three-dimensional far-field radiation patterns from reduced-sample measurements. By exploiting the plane-wave spectrum representation together with the asymptotic relations governing far-field behavior, the approach identifies a minimal yet sufficient set of sampling points determined by the antenna aperture size. An iterative interpolation procedure in the spectral domain is then employed to recover the missing field information and reconstruct the complete radiation pattern.

Numerical simulations show that the method recovers the main beam and dominant sidelobe features while requiring only a small fraction of conventional measurement data, approximately 3.7% in the example considered. The reconstructed patterns agree with full-wave reference solutions, and experimental results confirm robustness under practical measurement conditions.

The algorithm converges rapidly and incurs negligible computational cost relative to overall acquisition time, making it suitable for integration into measurement workflows where reducing scan duration is essential. To support reproducibility and further development, the full implementation in Julia programming language–including preprocessing routines, reconstruction scripts, and visualization tools–is openly released on GitHub.

Acknowledgments

The author gratefully acknowledges the support of Larry Chiu and Ohmplus Technology for providing simulated radiation pattern data for the standard gain horn and assistance with the measurement process.

References

[1] PARINI, C., GREGSON, S. F., MCCORMICK, J., et al. *Theory and Practice of Modern Antenna Range Measurements*. London (UK): IET, 2014. DOI: 10.1049/PBEW055E

[2] FOEGELLE, M. D. Antenna pattern measurement: Concepts and techniques. *Compliance Engineering*, 2002, vol. 19, no. 3, p. 22–33.

[3] ELSHERBENI, A. Z., INMAN, M. J. Antenna design and radiation pattern visualization. *Applied Computational Electromagnetics Society Journal*, 2003, vol. 18, no. 4, p. 26–32.

[4] NEWMAN, E., BOHLEY, P., WALTER, C. Two methods for the measurement of antenna efficiency. *IEEE Transactions on Antennas and Propagation*, 1975, vol. 23, no. 4, p. 457–461. DOI: 10.1109/TAP.1975.1141114

[5] GEYI, W. The method of maximum power transmission efficiency for the design of antenna arrays. *IEEE Open Journal of Antennas and Propagation*, 2021, vol. 2, p. 412–430. DOI: 10.1109/OJAP.2021.3066310

[6] SAUNDERS, S. R., ARAGON-ZAVALA, A. A. *Antennas and Propagation for Wireless Communication Systems*. 3rd ed. Chichester (UK): John Wiley & Sons, 2024. ISBN: 9781394223046

[7] CERNY, O., DOLECEK, R., KOPECKY, P., et al. Optimization of far-field antenna range. *Radioengineering*, 2015, vol. 24, no. 4, p. 892–897. DOI: 10.13164/re.2015.0892

[8] DEFORD, J. F., GANDHI, O. P. Phase-only synthesis of minimum peak sidelobe patterns for linear and planar arrays. *IEEE Transactions on Antennas and Propagation*, 1988, vol. 36, no. 2, p. 191–201. DOI: 10.1109/8.1096

[9] HANSEN, R. C. *Phased Array Antennas*. 2nd ed. Hoboken (USA): John Wiley & Sons, 2009. ISBN: 9780470401026

[10] TODNATEE, S., PHONGCHAROENPANICH, C. Iterative GA optimization scheme for synthesis of radiation pattern of linear array antenna. *International Journal of Antennas and Propagation*, 2016, vol. 2016, p. 1–8. DOI: 10.1155/2016/7087298

[11] ALLARD, R. J., WERNER, D. H., WERNER, P. L. Radiation pattern synthesis for arrays of conformal antennas mounted on arbitrarily-shaped three-dimensional platforms using genetic algorithms. *IEEE Transactions on Antennas and Propagation*, 2003, vol. 51, no. 5, p. 1054–1062. DOI: 10.1109/TAP.2003.811510

[12] MARCANO, D., DURAN, F. Synthesis of antenna arrays using genetic algorithms. *IEEE Antennas and Propagation Magazine*, 2000, vol. 42, no. 3, p. 12–20. DOI: 10.1109/74.848944

[13] CHOU, H.-T. An efficient successive projection method for the synthesis of phased array antennas to radiate contoured field patterns. In *Proceedings of the IEEE International Conference on Wireless Information Technology and Systems (ICWITS)*. Maui (HI, USA), 2012, p. 1–4. DOI: 10.1109/ICWITS.2012.6417699

[14] VERDIN, B., DEBROUX, P. 2D and 3D far-field radiation patterns reconstruction based on compressive sensing. *Progress In Electromagnetics Research M*, 2016, vol. 46, p. 47–56. DOI: 10.2528/PIERM15110306

[15] GU, Y., SUN, H.-H., VAN DER WEIDE, D. W. A near-field super-resolution network for accelerating antenna characterization. *IEEE Transactions on Antennas and Propagation*, 2024, vol. 73, no. 3, p. 1732–1742. DOI: 10.1109/TAP.2024.3511040

[16] PENG, F., LIU, X., ZHENG, J., et al. An effective method for antenna radiation pattern reconstruction based on phaseless measurement in a reverberation chamber. *IEEE Transactions on Antennas and Propagation*, 2023, vol. 71, no. 6, p. 4747–4758. DOI: 10.1109/TAP.2023.3262966

[17] GREGSON, S., MCCORMICK, J., PARINI, C. *Principles of Planar Near-Field Antenna Measurements*. London (UK): IET, 2007. ISBN: 0863417361

[18] PIZZO, A., SANGUINETTI, L., MARZETTA, T. L. Fourier plane-wave series expansion for holographic MIMO communications. *IEEE Transactions on Wireless Communications*, 2022, vol. 21, no. 9, p. 6890–6905. DOI: 10.1109/TWC.2022.3152965

[19] YAGHJIAN, A. D. An overview of near-field antenna measurements. *IEEE Transactions on Antennas and Propagation*, 1986, vol. 34, no. 1, p. 30–45. DOI: 10.1109/TAP.1986.1143727

[20] HANSEN, T. B., YAGHJIAN, A. D. *Plane-Wave Theory of Time-Domain Fields: Near-Field Scanning Applications*. New York (USA): John Wiley & Sons, 1999. ISBN: 9780470545522

[21] LIU, J. W., TSENG, S. H. Near-to-far-field transformation scheme utilizing a modified sinc interpolation method for PSTD simulations. *Optics Express*, 2024, vol. 32, no. 26, p. 47225–47235. DOI: 10.1364/OE.546322

[22] LU, Y., SHI, S., CUI, M., et al. Probe distance error analysis for phased array calibration based on BTM. *Microwave and Optical Technology Letters*, 2022, vol. 64, no. 3, p. 496–499. DOI: 10.1002/mop.33150

[23] HANSEN, J. E. (ed.). *Spherical Near-Field Antenna Measurements*. London (UK): Peter Peregrinus, 1988. DOI: 10.1049/PBEW026E

[24] AMIDROR, I. Scattered data interpolation methods for electronic imaging systems: A survey. *Journal of Electronic Imaging*, 2002, vol. 11, no. 2, p. 157–176. DOI: 10.1117/1.1455013

[25] ITOH, K. Analysis of the phase unwrapping algorithm. *Applied Optics*, 1982, vol. 21, no. 14, p. 2470–2470. DOI: 10.1364/AO.21.002470

[26] LIU, J. W. *Sparse Far-Field Reconstruction in the Spectral Domain* (Julia source code). [Online] Cited 2026-01-01. Available at: https://github.com/jake-w-liu/kinterp.jl

About the Authors . . .

Jake W. LIU was born in Hualien, Taiwan, in 1995. He received the B.S. degree in Electrical Engineering from National Taiwan University, Taipei, Taiwan, in 2017, and the Ph.D. degree from the Graduate Institute of Communication Engineering at the same university in 2022. His research interests include antenna measurement theory, calibration of phased arrays at millimeter-wave frequencies, and computational electromagnetics. He is currently an Assistant Professor in the Department of Electronic Engineering at National Taipei University of Technology.

Appendix A: Iterative Spectral-Domain Reconstruction Algorithm

The full implementation of the reconstruction procedure is available as open-source Julia code on GitHub [26]. Algorithm 1 summarizes the iterative spectral-domain method used in this work, following the same steps as the reference implementation, including spectral sampling, scattered-data interpolation, bicubic smoothing, and data-consistency enforcement at measured angular locations.

Algorithm 1. Iterative reconstruction algorithm.

Require: Frequency f, aperture (L_x, L_y), angular steps $(\Delta\theta, \Delta\phi)$, reduced FF samples $E_\theta^{\text{meas}}, E_\phi^{\text{meas}}$ on set $\mathcal{M}$
Ensure: Reconstructed far field E_θ, E_ϕ on $\mathcal{F} = \mathcal{M} \cup \mathcal{R}$
Compute $\lambda = c/f$, $k_0 = 2\pi/\lambda$, set $\Delta x = \Delta y = \lambda/2$
Determine $N_x = \lceil L_x/\Delta x \rceil$, $N_y = \lceil L_y/\Delta y \rceil$, $N_a = \max(N_x, N_y)$
Set $N_x^{\text{e}} = N_y^{\text{e}} = 2N_a + 1$; build $(k_{x,m}, k_{y,n})$
Form angular grid $(\theta_\mathcal{F}, \phi_\mathcal{F})$; compute $(k_x^{(s)}, k_y^{(s)})$ via (1)
Tabulate measured data on $(\theta_\mathcal{F}, \phi_\mathcal{F})$
Compute (θ_{mn}, ϕ_{mn}) from $(k_{x,m}, k_{y,n})$
Build $\mathbf{M}$ on $(\theta_\mathcal{F}, \phi_\mathcal{F})$ with ones on $\mathcal{M}$; set $\mathbf{I} = 1 - \mathbf{M}$
Convert $(E_\theta^{\text{meas}}, E_\phi^{\text{meas}})$ to $\mathcal{E}_\xi^{(0)}(\theta_\mathcal{F}, \phi_\mathcal{F})$ using (6)
Initialize $p = 0$, set $\mathcal{E}_\xi^{(p)}(\theta_\mathcal{F}, \phi_\mathcal{F}) = \mathcal{E}_\xi^{(0)}(\theta_\mathcal{F}, \phi_\mathcal{F})$ (first pass assigns measured values to $\mathcal{M}$ and zeros elsewhere)
while $p \le p_{\max}$ **and** not converged **do**
    Extract magnitudes and unwrapped phases of $\mathcal{E}_\xi^{(p)}$
    Scattered interpolation from $(k_x^{(s)}, k_y^{(s)})$ to $(k_{x,m}, k_{y,n})$
    Reconstruct $\mathcal{E}_\xi$ on $(k_{x,m}, k_{y,n})$
    Bicubic interpolation back to $(\theta_\mathcal{F}, \phi_\mathcal{F})$ to obtain $\mathcal{E}_\xi^{(p+1)}$
    Enforce measurement consistency via (13)
    Compute cost using (14); check convergence
    $p \leftarrow p + 1$
end while
Map final spectral components to far field via (6), convert to (E_θ, E_ϕ)
return E_θ, E_ϕ